Geophysical Journal International

Geophys. J. Int. (2016) **205,** 243–256 doi: 10.1093/gji/ggw004

GJI Geomagnetism, rock magnetism and palaeomagnetism

Increasing the resolution and the signal-to-noise ratio of magnetic resonance sounding data using a central loop configuration

Ahmad A. Behroozmand,[1] Esben Auken,[2] Gianluca Fiandaca[2] and Simon Rejkjaer[2]

[1] *Department of Geophysics, Stanford University, Stanford, CA, USA. E-mail: abehrooz@stanford.edu*

[2] *Department of Geoscience, Aarhus University, Aarhus, Denmark*

Accepted 2016 January 5. Received 2015 October 5; in original form 2015 March 27

SUMMARY

Surface nuclear magnetic resonance technique, also called magnetic resonance sounding (MRS), is an emerging geophysical method that can detect the presence and spatial variations of the subsurface water content directly. In this paper, we introduce the MRS central loop geometry, in which the receiver loop is smaller than the transmitter loop and placed in its centre. In addition, using a shielded receiver coil we show how this configuration greatly increases signal-to-noise ratio and improves the resolution of the subsurface layers compared to the typically used coincident loop configuration. We compare sensitivity kernels for different loop configurations and describe advantages of the MRS central loop geometry in terms of superior behaviour of the sensitivity function, increased sensitivity values, reduced noise level of the shielded receiver coil, improved resolution matrix and reduced instrument dead time. With no extra time and effort in the field, central-loop MRS makes it possible to reduce measurement time and to measure data in areas with high anthropogenic noise. The results of our field example agree well with the complementary data, namely airborne electromagnetics, borehole data, and the hydrologic model of the area.

Key words: Electromagnetic theory; Magnetic and electrical properties; Hydrogeophysics.

INTRODUCTION

Surface nuclear magnetic resonance (surface NMR) is an emerging geophysical method used for direct investigation of near-surface aquifers. The interaction between an applied magnetic field (generated using a surface based wire-loop transmitter) and magnetic moments of protons in the subsurface water molecules makes it possible to record a water-solely driven signal from the ground surface, that is non-invasively. Consequently, direct determination of the (free) water content and an estimation of pore size distribution are obtained. For 1-D applications, the method is referred to as magnetic resonance sounding or MRS. We will use this term in our paper.

Naturally, protons in groundwater are at their thermal equilibrium state with the Earth's static magnetic field ($\mathbf{B}_E$) and precess about it at the local Larmor frequency $f_L = -\gamma B_E/2\pi$, where $\gamma = 2.675 \times 10^8$ s^{-1} T^{-1} is the proton gyromagnetic ratio. Therefore, each small volume of the soil in the subsurface, fully or partially saturated with water, acquires a so-called net magnetic moment aligned in the same direction as the background field. The Magnetic resonance occurs by passing a tuned AC pulse (with intensity of up to around 800 A, a duration of 20–40 ms and a frequency tuned to the local Larmor frequency) through a large wire loop deployed on ground surface that generates a strongly heterogeneous energizing magnetic field in the subsurface. As a consequence, at each position the effective component (i.e. perpendicular to $\mathbf{B}_E$) of the energizing field tips the magnetization away from its equilibrium position, meaning that it rotates a component of the net magnetization into a plane transverse to $\mathbf{B}_E$. Unlike laboratory NMR, the tip angle here is spatially varying. After the energizing pulse is terminated, the continued precessional motion of the tipped magnetizations produces a secondary magnetic field that is recorded inductively using a wire loop on the surface. This experiment is called a free induction decay (FID) and is the most common MRS measurement. In the standard MRS measurement, FIDs are recorded for a number of energizing pulse intensities by which different Earth volumes are excited. The initial amplitude of a decaying FID signal is directly linked to the amount of water probed, while its decay rate provides information of the pore sizes. These parameters allow an empirical relation to hydrologic parameters of interest, for instance hydraulic conductivity. For a comprehensive overview of the MRS method see, for example, Weichman *et al*. (2000), Hertrich (2008) and Behroozmand *et al*. (2015).

One of the main challenges in measuring MRS data in many places of interest is that these are often contaminated with anthropogenic noise and the fact that the method has a relatively low signal-to-noise ratio (S/N). The magnetic resonance of the subsurface water molecules within the weak geomagnetic field (with intensity of ~25–65 micro-Tesla) produces a 100-nv-scale measurable signal. This signal level is in most cases (much) lower than the

noise level, which suggests recording multiple signals and stacking them together to increase S/N. MRS data is typically acquired using a coincident loop configuration, that is the same wire loop is employed to transmit the energizing pulse and receive the NMR signal. It is generally favourable to increase the transmitter loop size since it helps to probe deeper Earth (for more information about the extent to which increasing loop size will increase investigation depth see, e.g. Müller-Petke & Yaramanci 2008; Behroozmand *et al*. 2013a).

The goal of this paper is to introduce a measurement configuration that increases S/N and improves resolution of the estimated model. We show results of central-loop MRS data and discuss advantages of this configuration compared with the typical coincident loop configuration. We also show how shielding the receiver loop reduces the spike and noise level. We present sensitivity kernels of different loop configurations, discuss superior behaviour of the central loop kernel in terms of sensitivity structure and amplitude and compare noise data acquired at different sites using both coincident and central loop geometries. In addition, model resolutions of the two configurations are studied through resolution matrices and synthetic examples. Finally, the results of our field example is presented and compared with complementary information as well as with borehole data and hydrologic data from the area.

CENTRAL VERSUS COINCIDENT LOOP MRS

MRS measures an average of the distribution of water in the subsurface. For FID measurements, the MRS forward response is generally described by

$$V(q,t) = \int K(q,\boldsymbol{r}) \int W(\boldsymbol{r},T_2^*)\cdot \mathrm{e}^{-\frac{t}{T_2^*}}\,\mathrm{d}T_2^*\,d^3\boldsymbol{r}, \tag{1}$$

in which the MRS kernel function, under on-resonance conditions, is described as

$$\begin{aligned} K(q,\boldsymbol{r}) = &-\omega_L M_0 \sin\left(\gamma \frac{q}{I_0}\left|\boldsymbol{B}_T^+(\boldsymbol{r})\right|\right) \\ &\times \frac{2}{I_0}\left|\boldsymbol{B}_R^-(\boldsymbol{r})\right|\cdot e^{i[\zeta_T(r,\omega_L)+\zeta_R(r,\omega_L)]} \\ &\times \Big[\hat{\boldsymbol{b}}_R^{\perp}(\boldsymbol{r},\omega_L)\cdot\hat{\boldsymbol{b}}_T^{\perp}(\boldsymbol{r},\omega_L) + i\hat{\boldsymbol{b}}_0\cdot\hat{\boldsymbol{b}}_R^{\perp}(\boldsymbol{r},\omega_L) \\ &\times \hat{\boldsymbol{b}}_T^{\perp}(\boldsymbol{r},\omega_L)\Big]. \end{aligned} \tag{2}$$

In eq. (1), $q = I_0\cdot\tau_p$ is the transmitter pulse moment (as the product of the current amplitude, I_0, and pulse duration, τ_p), $V(q,t)$ denotes the induced voltage as a function of pulse moment and time, and $W(\boldsymbol{r},T_2^*)$ is the water content distribution as a function of the position, $\boldsymbol{r}$, and the effective transverse relaxation time, T_2^*. In eq. (2), $K(q,\boldsymbol{r})$ denotes the MRS kernel function, also called the sensitivity function, $\omega_L = 2\pi f_L$ is the angular Larmor frequency, and M_0 and γ are the net magnetization at thermal equilibrium state and the proton gyromagnetic ratio, respectively. $\boldsymbol{B}_T^+(\boldsymbol{r})$ and $\boldsymbol{B}_R^-(\boldsymbol{r})$ are the effective components of the transmitter and receiver fields. The + and – superscripts denote the co- and counter-rotating components of the projected fields onto the plane perpendicular to $\boldsymbol{B}_E$. Similarly, ζ_T and ζ_R are the phase delays (due to the conductivity effects) between the transmitter and receiver loops to the observation point, $\boldsymbol{r}$. Finally, the last line in eq. (2) describes the directional dependency of the kernel on the transmitter, the receiver and the Earth's fields. $\hat{\boldsymbol{b}}_0$, $\hat{\boldsymbol{b}}_T^{\perp}$ and $\hat{\boldsymbol{b}}_R^{\perp}$ are the unit vectors of $\boldsymbol{B}_E$, $\boldsymbol{B}_T^{\perp}$ and $\boldsymbol{B}_R^{\perp}$, that is the components of the transmitter and receiver field perpendicular to $\boldsymbol{B}_E$.

Let's take a closer look at the kernel function. Eq. (2) gives an insight into the resolution characteristics of different loop configurations. It describes how intensity and orientation of the magnetic fields of the transmitter and receiver loops contribute to the measured signal. The amplitude of the co-rotating component of the transmitter field and the pulse moment determine the tip angle at each position $\boldsymbol{r}$. Moreover, the amplitude of the counter-rotating component of the receiver field scales the signal amplitude. In conductive media, propagation of the EM fields causes a phase delay from the transmitter to the observation point and from the observation point to the receiver, described by the exponential function in the second line of eq. (2). The third line in eq. (2) includes the unit vectors of the transmitter, receiver, and the Earth's field and takes into account the directional dependency of the signal, that is the dependency on the direction of transmitter and receiver fields and their orientation with respect to $\boldsymbol{B}_E$. For coincident loop configuration, $\boldsymbol{B}_T = \boldsymbol{B}_R$, $\zeta_T = \zeta_R$ and the third line of eq. (2) is equal to 1. This means that for a conductive ground, considering an on-resonance excitation, the imaginary component of the scalar-valued kernel is caused solely by ground conductivity. In other words, for an infinitely resistive Earth, the kernel function is real valued and for a conductive Earth the kernel is complex valued. If the transmitter and receiver loops do not coincide, that is are separated, the third line of eq. (2) contributes to the imaginary component of the kernel as well. Therefore, even for a resistive Earth and an on-resonance excitation, the kernel function is generally complex valued. For more information about behaviour of the MRS kernel function see, for example, Weichman *et al*. (2000), Hertrich (2008) and Behroozmand *et al*. (2015).

For 1-D applications, the MRS kernel in eq. (1) is integrated over x and y, and for each pulse moment is presented as a 1-D function with depth ($K(q,z)$). For a given configuration and pulse moment, a 1-D kernel represents the sensitivity of the data to different depth intervals.

Although less common, separated loop geometries have been used for collecting surface-NMR data. For instance, Hertrich *et al*. (2009) and Jiang *et al*. (2015) used, respectively, multi-offset loops and elongated transmitter and in-loop receiver arrays for 2-D surface NMR investigations and concluded that these configurations provide better resolution for shallow depths.

In this study, we seek a loop geometry that increases S/N and the resolution of the entire probed subsurface, compared with the typical coincident loop configuration. As a first consideration, we want to use a large transmitter loop. Not only because it will help to probe deeper, but also because its larger sampling volume at each depth interval (inversion layer) provides a better average sensitivity of that layer, that is a more representative estimate of a 1-D model is achieved. Therefore, throughout this study, we used a 100-m-side square loop as transmitter for our synthetic and field examples.

Consequently, our study focused on assessing the sensitivity of different separated loop configurations that is of receiver loops with different sizes and positions from that of the transmitter loop. The assessment was carried out firstly by comparing behaviour and level of the separated-loop versus coincident-loop kernels to find an optimal configuration that helps increase S/N. To highlight larger depth sampling and higher kernel values of the proposed configuration, as compared with other separated-loop configurations, Fig. 1 displays 1-D kernel-amplitude structures for different coincident, central and other separated loop configurations. The kernel calculations were

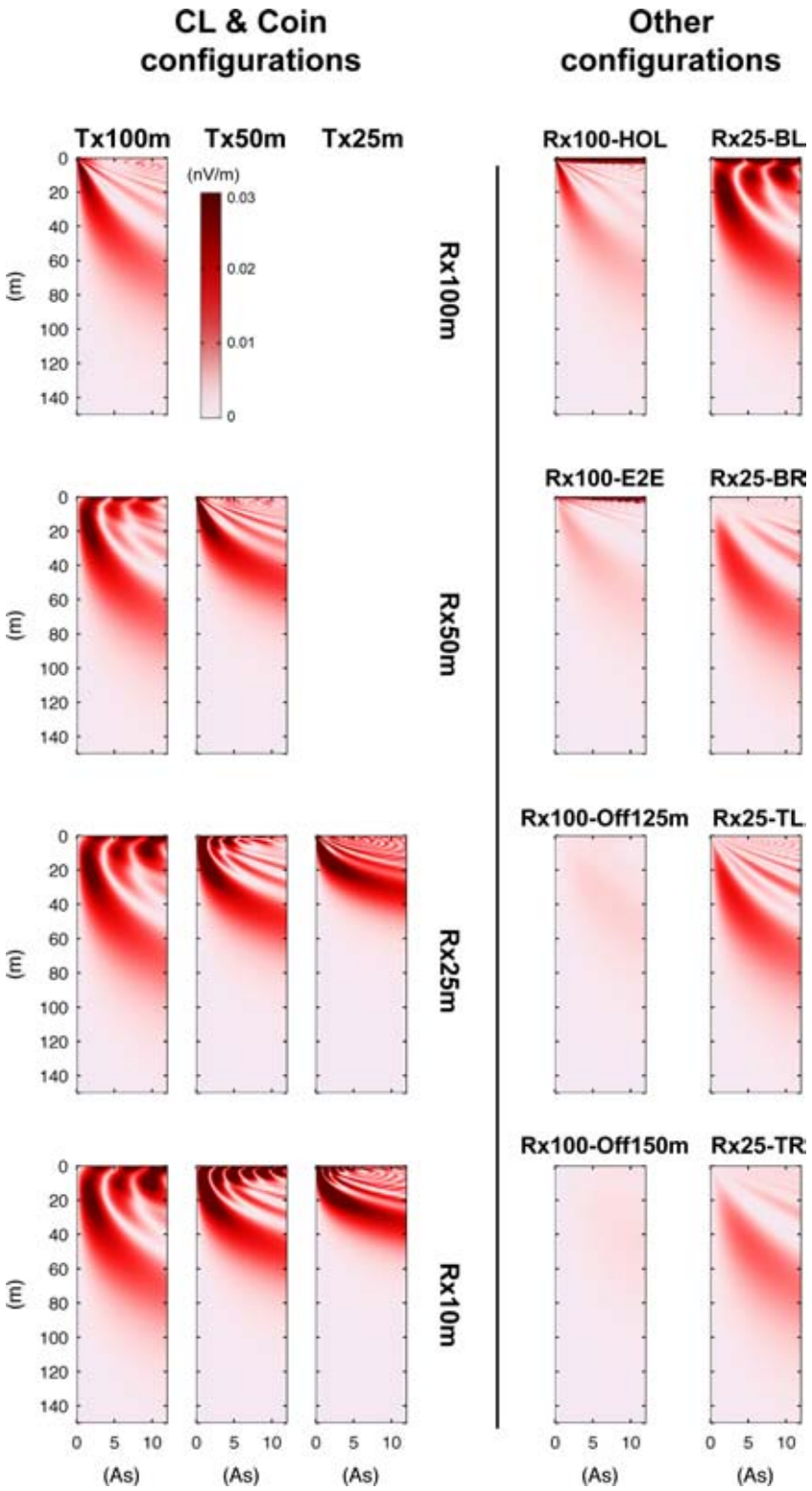

Figure 1. Comparison of 1-D kernel-amplitude structures for different loop configurations. The left-hand panels display kernels of coincident and central loop configurations using different transmitter loop sides of 100 m (column 1), 50 m (column 2) and 25 m (column 3) and different receiver loop sides of 100 m (row 1), 50 m (row 2), 25 m (row 3) and 10 m (row 4). For the right-hand panels we used a 100-m-side transmitter loop. Column 4 shows kernels of half overlapped (HOL), edge-to-edge (E2E) and offset (with 125 m and 150 m loop separation) configurations using a 100-m-side receiver loop. Column 5 shows kernels from non-central in-loop configurations using a 25-m-side receiver loop placed at the bottom-left (BL), bottom-right (BR), top-left (TL) and top-right (TR) corners of the transmitter loop (with 0.5-m loop separation). The kernels are normalized to the receiver loop effective area for comparison. For information about the model and field setup see the text.

made numerically for a homogeneous half-space model with a resistivity value of 100 Ωm, and at Earth's field intensity and inclination of 47 960 nT and 60°, respectively. On the left, kernel amplitudes for coincident and central loop configurations using different transmitter (100, 50 and 25 m) and receiver (100, 50, 25 and 10 m) loop sizes are presented. On the right, we use a 100-m transmitter and show kernels for other separated-loop configurations. Those include half-overlapped (HOL), edge-to-edge (E2E) and offset (with 125- and 150-m loop separation) loops using a 100-m receiver loop. Moreover, the rightmost column displays kernels for non-central in-loop

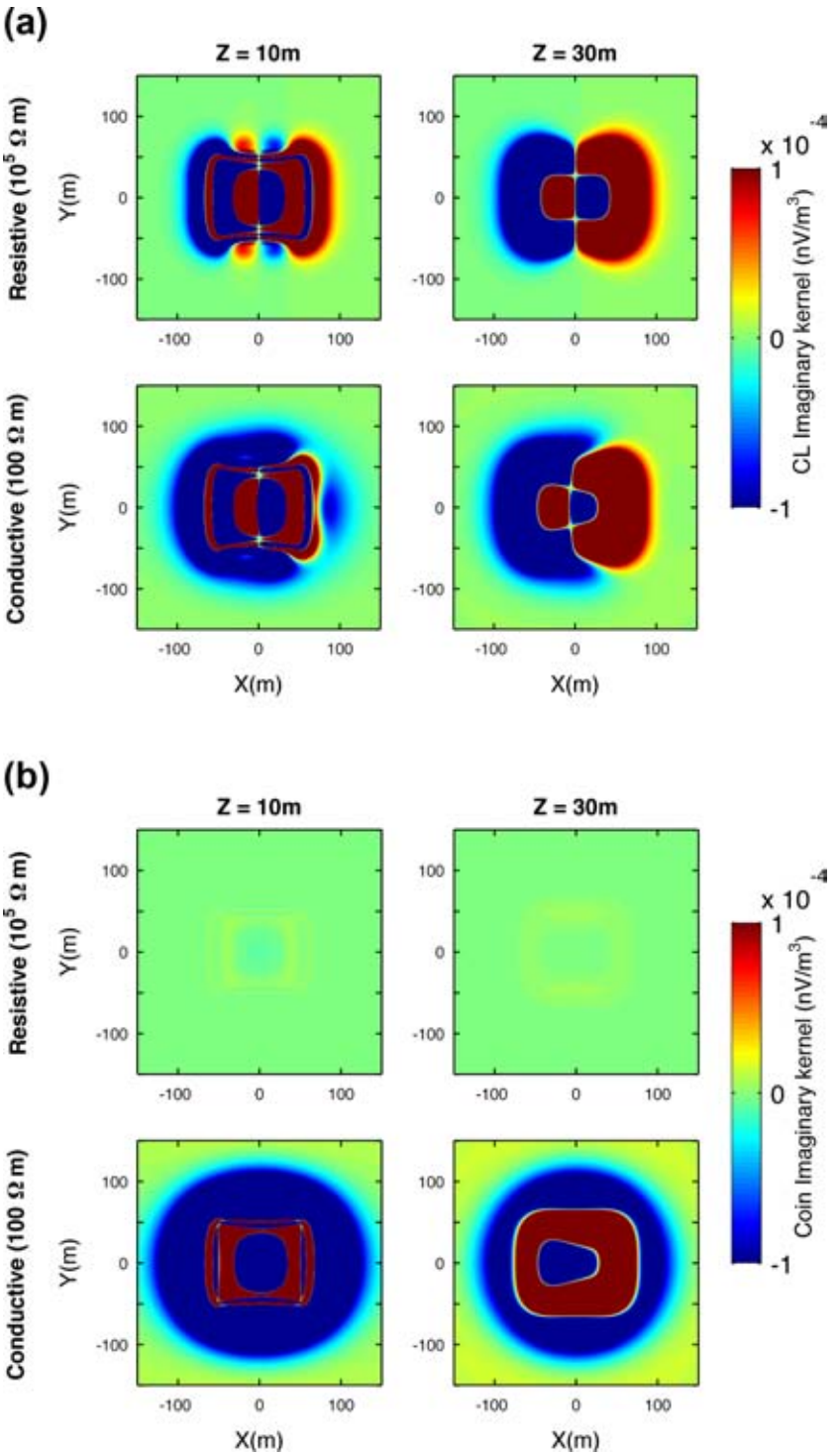

Figure 2. Numerical simulations of the imaginary components of the central-loop (a) and coincident-loop (b) 3-D kernels for a resistive (10^5 Ωm homogeneous half-space, row 1) and a conductive (100 Ωm homogeneous half-space, row 2) Earth. Columns 1 and 2 show horizontal (*x*–*y*) slices through the 3-D kernel at depths 10 and 30 m, respectively. (a) The kernels are simulated for a one-turn square loop (100-m side length) as a transmitter, a four-turn square loop (25-m side length) as a receiver. (b) The kernels are simulated for a one-turn square loop (100-m side length) as a transmitter and a receiver. A pulse moment value of 3.28 As is used and the Earth's field intensity and inclination were set to 47 960 Hz and 60°, respectively.

configurations using a 25-m receiver loop placed at the bottom-left (BL), bottom-right (BR), top-left (TL) and top-right (TR) corners of the transmitter loop (with 0.5-m loop separation). Comparing kernels of different configurations demonstrates that larger depth samplings are achieved when using a 100-m transmitter loop and higher amplitudes are obtained when using a 25-m receiver loop (row 3 and column 1). It has been tested but not shown here that using a smaller receiver loop does not increase the sampling interval and/or the kernel amplitude. It is noteworthy that if we use a smaller transmitter loop (e.g. 50-m side length) in a central loop configuration, besides reduced depth of investigation, the number of oscillation in the kernel will increase and their sensitive zones (energy) will move to the very shallow subsurface. Moreover, we observe that placing a receiver coil at the bottom-left corner of the transmitter loop (1st row, 5th column) results in increased sampling interval and kernel amplitude that is comparable to those from the central loop configuration. However, we prefer the central loop configuration because of its simplicity.

The separated-loop MRS kernel has a complicated spatial distribution and, as already mentioned, even for a resistive Earth it is generally complex valued. A central-loop kernel, however, possesses an interesting feature in the integration plane. For resistive Earth, its imaginary component contains a symmetric feature (with opposite signs), as shown in Fig. 2(a), row 1. Therefore, for 1-D applications, when the central loop kernel function is integrated over the horizontal depth planes (over *x*- and *y*-axes), it becomes real valued. On the contrary, for conductive Earth the imaginary central-loop kernel no longer holds this feature and the 1-D kernel becomes complex (see Fig. 2a, row 2). This is an advantage of the central loop configuration, because its geometry-driven kernel helps improve subsurface resolution (Weichman *et al*. 2000; Braun *et al*. 2005; Legchenko *et al*. 2008). For comparison, Fig. 2(b) shows the same kernel plots for the coincident loop configuration.

Fig. 3 compares behaviour of coincident-loop and central-loop 1-D kernels. The kernels are calculated for the same model and field setup used in Fig. 1. Then the kernel function was integrated in horizontal directions to provide a 1-D function. Grey and black curves display real (row 1) and imaginary (row 2) components of the coincident- and central-loop 1-D kernels, respectively. The kernels are plotted for small (1 As), intermediate (5 As) and large (10 As) pulse moments. Note that the kernels are normalized to the receiver loop effective area.

As for the coincident-loop kernel, it is evident that the peak of sensitivity (for both real and imaginary components) penetrates deeper as pulse moments are increased. Moreover, the real components of the kernel (row 1) are oscillatory near the surface, that is prior to the main sensitive zone. Therefore, each pulse moment produces a sensitivity function that is sensitive to a certain depth interval. As a result, the shallower parts are mainly sensitive to smaller pulse moments and the deeper parts are mainly sensitive to higher pulse moments.

As for the central-loop kernel, a noticeable difference is that the real and imaginary components alternate their sign over the range of pulse moments, with significantly higher amplitudes than those of coincident-loop kernel. Moreover, for a given pulse moment, they

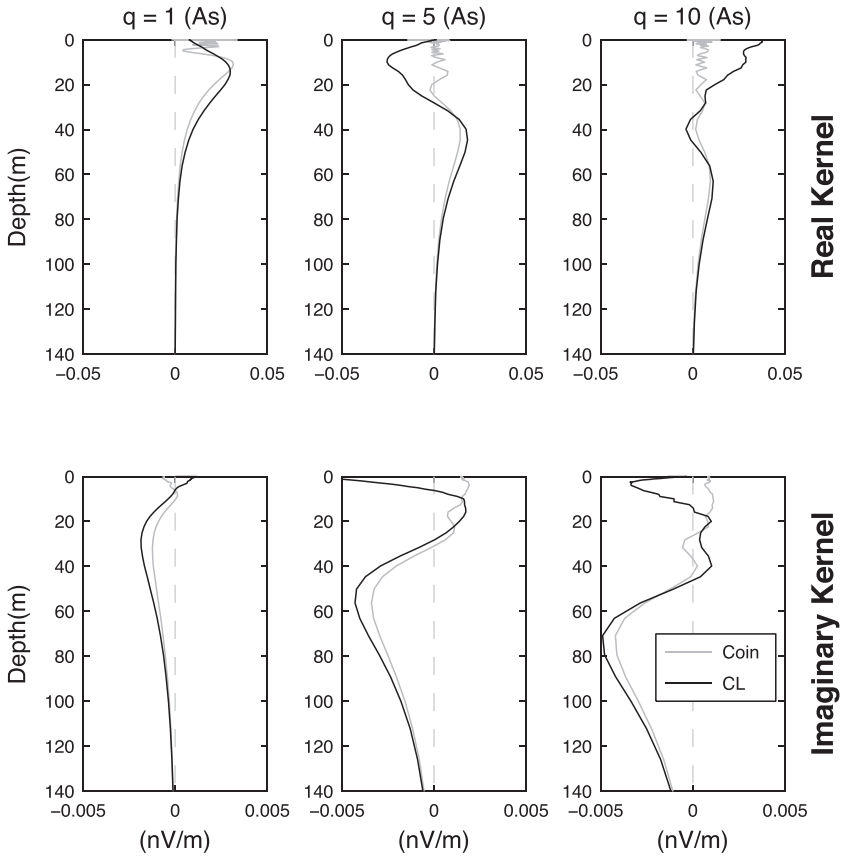

Figure 3. Numerical simulations of the coincident- (grey) and central-loop (black) 1-D kernels for a 100 Ωm homogeneous half-space at pulse moment values of 1 As (column 1), 5 As (column 2) and 10 As (column 3). Rows 1 and 2 display real and imaginary components of the kernels, respectively. The kernel values are normalized for comparison. The same field setup as in Fig. 2 was used for simulations.

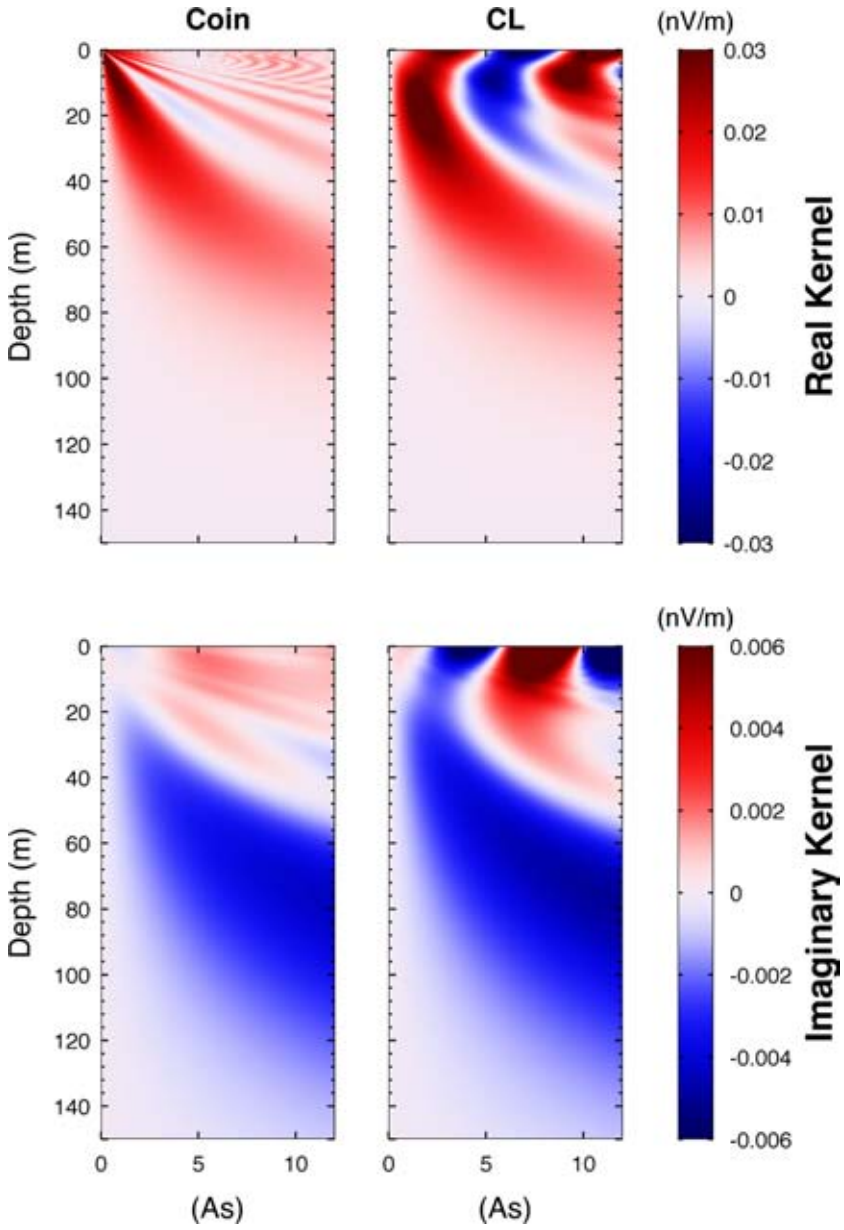

Figure 4. Numerical simulations of the coincident- (column 1) and central-loop (column 2) 1-D kernels as a function of pulse moment and depth, for a 100 Ωm homogeneous half-space. Rows 1 and 2 display real and imaginary components of the kernels, respectively. The kernel values are normalized for comparison. The same field setup as in Fig. 2 was used for simulations.

probe larger depth intervals (Davis & Macnae 2012; Behroozmand *et al*. 2013b). The real central-loop kernels overlay the coincident loop kernel peaks, with peak amplitudes that are as large as or larger than those of the coincident kernel. Moreover, they present a relatively large sensitivity in the shallower parts with no presence of the destructive oscillatory feature observed for the coincident-loop kernels. The imaginary central-loop kernels (bottom row) also present higher amplitudes throughout the pulse moments as well as in depth. This behaviour of the central-loop 1-D kernel is superior to that of coincident loop because it increases S/N and provides a better resolution of the subsurface when both components form the data, as will be described later.

To obtain a better comparison between the coincident- and central-loop 1-D kernels, Fig. 4 shows 1-D kernel structures, that is 1-D kernel as a function of depth and pulse moment, for the same resistivity model and field setup used in Figs 1 and 3. Columns (1) and (2) show coincident- and central-loop kernel structures, respectively. The kernel values are normalized for comparisons. Again, as shown in panels of column (1), the coincident real kernel is the most sensitive to the shallow subsurface, that is at small pulse moments, (warm colours in the top left panel) while the imaginary kernel is mainly sensitive to the deeper subsurface (cold colour in the bottom left panel). As column (2) shows, generally, central loop real and imaginary kernels possess higher amplitudes both throughout the pulse moments and over larger depth intervals, which often results in higher signal amplitude. Moreover, unlike coincident kernel, central loop kernels contain additional sensitivity to the shallower subsurface.

Noise level

In the previous section, we showed the superior behaviour of central loop kernel over coincident loop kernel in terms of the kernel structure and sensitivity values. Another viewpoint, when seeking increased S/N, is to compare the noise levels in the receiver loops of the two configurations. In practice, effort is made in the field to place the transmitter and receiver loops in the best position with respect to the noise sources in the area (Dalgaard *et al*. 2014). However, it is often the case for environmental investigations to conduct MRS surveys in culturally developed areas, which makes it more difficult to suppress noise. Common practice is to use a figure-of-eight loop configuration (Trushkin *et al*. 1994) that helps increase S/N but, at the same time, leads to a significant reduction of the depth of investigation. In this study, we used a shielded receiver coil to reduce electromagnetic interference. Shielded receiver coils are commonly used in transient EM and are known to reduce the noise level significantly (Nyboe & Sørensen 2012). The shield reduces noise due to varying capacitive coupling to the conducting ground surface along the wire. The noise voltage produced between the receiver cable and ground results from man-made noise sources, for instance power poles or machineries connected to the ground. Generally, the electric field coupling can be modelled as a current generator connected between the receptor (here the receiver coil) and ground whose pick-up voltage depends on frequency of the noise source, resistance of the affected circuit to ground, capacitance between the conductors and voltage amplitude of the source. Shielding the receiver coil and grounding the shield results in reducing the capacitance between the conductors and picks up the varying electric charges (Ott 1988). It is also shown that this capacitive noise contribution highly depends on the moisture content in the vicinity of the coil (Nyboe & Sørensen 2012). We used a shielded 25-m-side 4-turn square loop as a receiver, consisting of four insulated copper conductors (0.75 mm in diameter) shielded using an aluminium foil (100 per cent shield coverage).

In order to assess the effect of shielding on the noise level, we collected noise data as shown in Fig. 5. The data were acquired using a two-channel instrument built to resemble a MRS system. For more information about the instrument see Dalgaard *et al*. (2014). Channel 1 was connected to a 25 × 25 m^2 shielded coil with 4 wire turns while a 400-m ordinary cable formed a 4-turn 25 × 25-m loop and was connected to channel 2. For direct comparison, the data were acquired synchronously and the loops were located at almost the same spot (1 m separation). The data were measured for 100 sec. Afterwards, to make the data comparable to field data recorded with the NUMIS Poly system, a digital bandpass filter, centred at 2100 Hz with a bandwidth of 150 Hz, was applied to the noise data. The data are shown in Fig. 5 as time series. Grey and black curves correspond to the data measured using the unshielded and shielded loops, respectively. As shown in the figure, the noise-reduction capability of the shielded coil is remarkable (here with a factor of five) and the noise ratio remains constant for the long durations. The inset of Fig. 5 shows a close-up view of the time series for the duration of 35–36 s. It is clear that the shield removes the spikes in the unshielded-coil data, which is caused by the current running on the surface of the ground (Kurt Sørensen, private communication, 2015).

In order to generalize this conclusion, we conducted a comprehensive noise-analysis survey during which we simultaneously measured the noise signal in the coincident (unshielded) and central (shielded) receiver loops at different sites. Fig. 6 shows the results of our noise analyses. The noise data were acquired at five different sites with different noise conditions. To obtain good statistics, a large number of noise data was recorded at each site as shown in rows of Fig. 6 (see the number of records on the panels of column 2). Each black dot in the panels of column (1) represents noise rms in the coincident receiver loop (*x*-axis) versus noise rms in the central receiver loop (*y*-axis); all normalized to the loop area. Grey lines show identity (one-to-one) lines. The noise amplitude in the central receiver loop is observed to be considerably lower than the noise amplitude in the coincident receiver loop. Column (2) in Fig. 6 displays histograms of the relative noise amplitudes at each site and clearly confirms lower amplitude of the noise recorded in the shielded central receiver loops (noise reduction factor of up to 2).

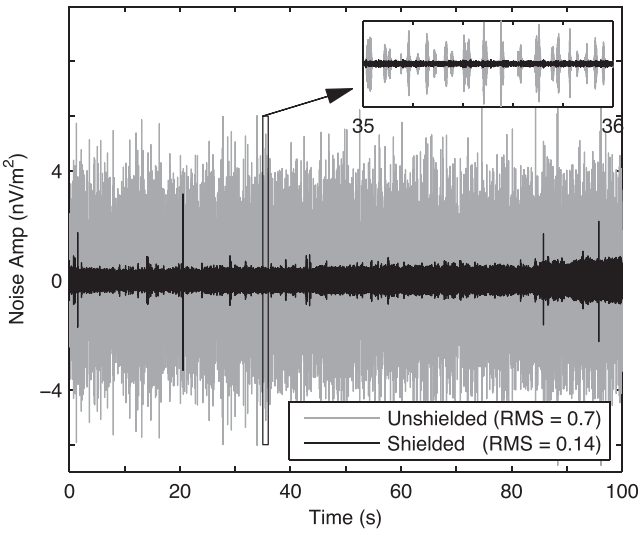

Figure 5. The effect of shielding on the noise level. Grey and black curves show area-normalized noise time series acquired using unshielded and shielded coils, respectively (loop effective areas: 25 × 25 × 4 m^2). The data are collected synchronously for 100 seconds and the loops were located at almost the same spot (1-m separation). The unshielded- and shielded-coil data have rms values of 0.7 and 0.14, respectively, which indicates a noise reduction factor of five. The inset shows a close-up view of the data for the duration of 35–36 s.

The result from our noise experiments is a very advantageous property of the central loop configuration with a shielded receiver loop, particularly in a noisy environment. The shielding could offer a similar reduction in noise as seen in Fig. 5, where the noise was recorded with our own instrument and where the coupling of the shield with the amplifier is better than what can be achieved with the Numis instrumentation.

Resolution comparison

So far, we showed that central loop configuration provides superior kernel in terms of kernel amplitude and that lower-amplitude noise contaminates the data, which both help increase S/N. From the inversion (or model space) point of view, it is also essential to assess the accuracy of the central-loop MRS parameter determination and compare it with that of coincident-loop data. In other words, the increased S/N property of the central-loop data gains higher value if it provides an equally good or better parameter determination compared with coincident-loop MRS data. We investigate this matter by means of resolution matrices and synthetic examples.

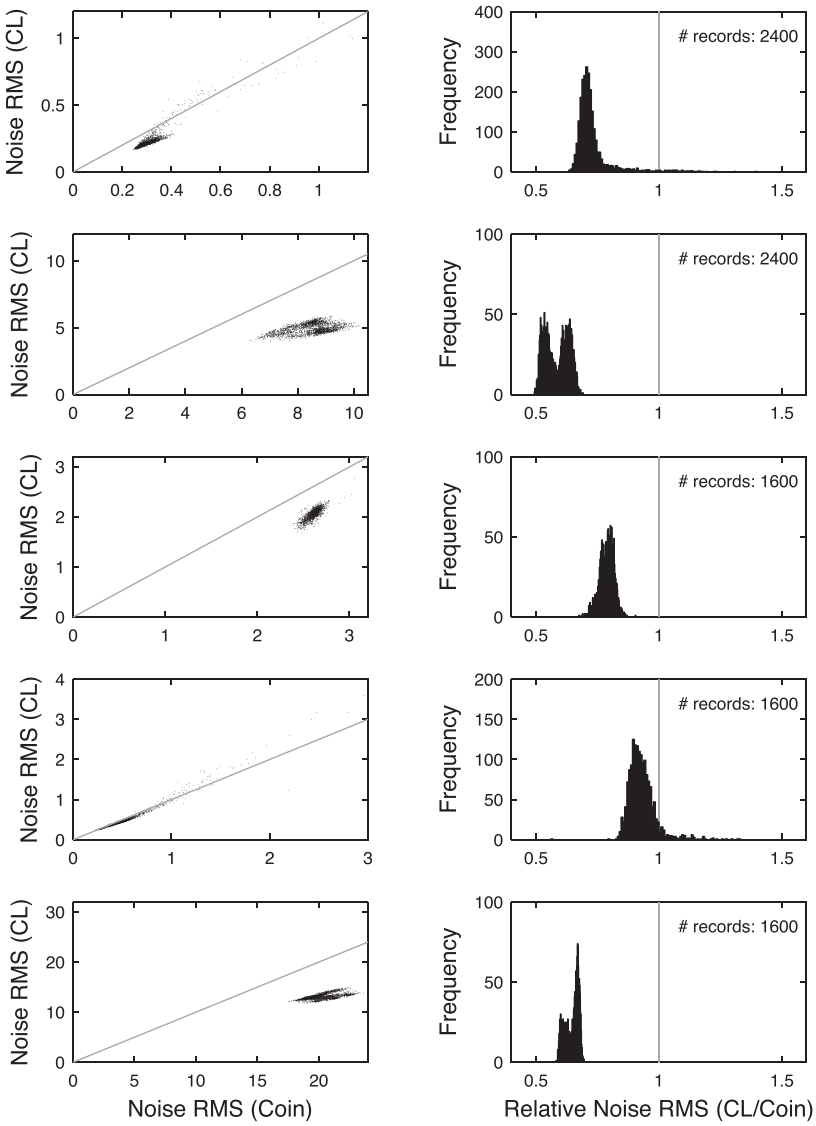

Figure 6. Analysis of noise data. The data were acquired simultaneously using a 100-m one-turn square loop (Coin) and a 25-m four-turn square loop (CL). Rows 1–5 show results of the noise data collected at different sites. Column 1: each back dot represents noise rms in the Coin loop (x-axis) versus the noise rms in the CL loop (y-axis). Noise data are normalized for comparison. Grey line shows identity line. Column 2: histograms of the data shown in column 1. The number of noise records at each site is displayed in the top right hand corner of each panel.

One way to realize how well an estimated solution ($\boldsymbol{m}^{\text{est}}$) compares to the true solution ($\boldsymbol{m}^{\text{true}}$) is by investigating the model resolution matrix $\boldsymbol{R}$; $\boldsymbol{m}^{\text{est}} = \boldsymbol{R}\boldsymbol{m}^{\text{true}}$. Hypothetically, if $\boldsymbol{R}$ is an identity matrix all of the model parameters are perfectly resolved. In practice, however, each row of $\boldsymbol{R}$ represents a weighted average of the true parameters and indicates how well each estimated model parameter is tied to the true one. Therefore, better resolutions are achieved when the peaks of the weighted average functions are sharp and centred about the main diagonal of $\boldsymbol{R}$. Being independent of the data, the resolution matrix describes theoretically how well the MRS kernel is able to resolve elements of $\boldsymbol{m}^{\text{est}}$.

Following Müller-Petke & Yaramanci (2008), Fig. 7 compares model resolution matrices driven from singular value decomposition (SVD) of the linear MRS forward operator (i.e. using initial-amplitude data) for coincident- and central-loop real (Fig. 7a) and complex (Fig. 7b) kernels; $\boldsymbol{K}_{MRS} = \boldsymbol{U}_p \boldsymbol{S}_p \boldsymbol{V}_p^T$. In doing this, the resolution matrix is given by $\boldsymbol{R} = \boldsymbol{V}_p \boldsymbol{V}_p^T$, where $\boldsymbol{V}$ is an $m \times m$ matrix (m being number of model parameters) of basis vectors associated with model space and T denotes matrix transpose. To give meaning to the sensitivity analysis of resolution matrices, we added 2 per cent Gaussian noise to real and imaginary data and calculated the kernels for densely sampled pulse moments and depths. In addition, we used the Picard plot (Fedi *et al*. 2005) to choose truncation level of the singular values used for analysis (denoted as the subscript p in the above-mentioned resolution matrix expression). For a given noise level, this type of analysis investigates theoretically the achievable amount of depth resolution. Again the same model and field setup as that of Fig. 2 was used for simulations. In Fig. 7, the truncated resolution matrices (row 1) of the two configurations are shown for real (a) and complex (b) data and for the kernel functions of Fig. 4. Row 2 in Fig. 7 shows the singular values (s_i), as grey curves, and the coefficient $|\boldsymbol{u}_i^T \boldsymbol{d}|/s_i$, as circles, for each configuration. Black lines indicate the truncation levels for which the resolution matrices are plotted in row 1. The truncation levels are determined based on the Picard plots, that indicate a range of singular values for which the coefficients $|\boldsymbol{u}_i^T \boldsymbol{d}|/s_i$ on

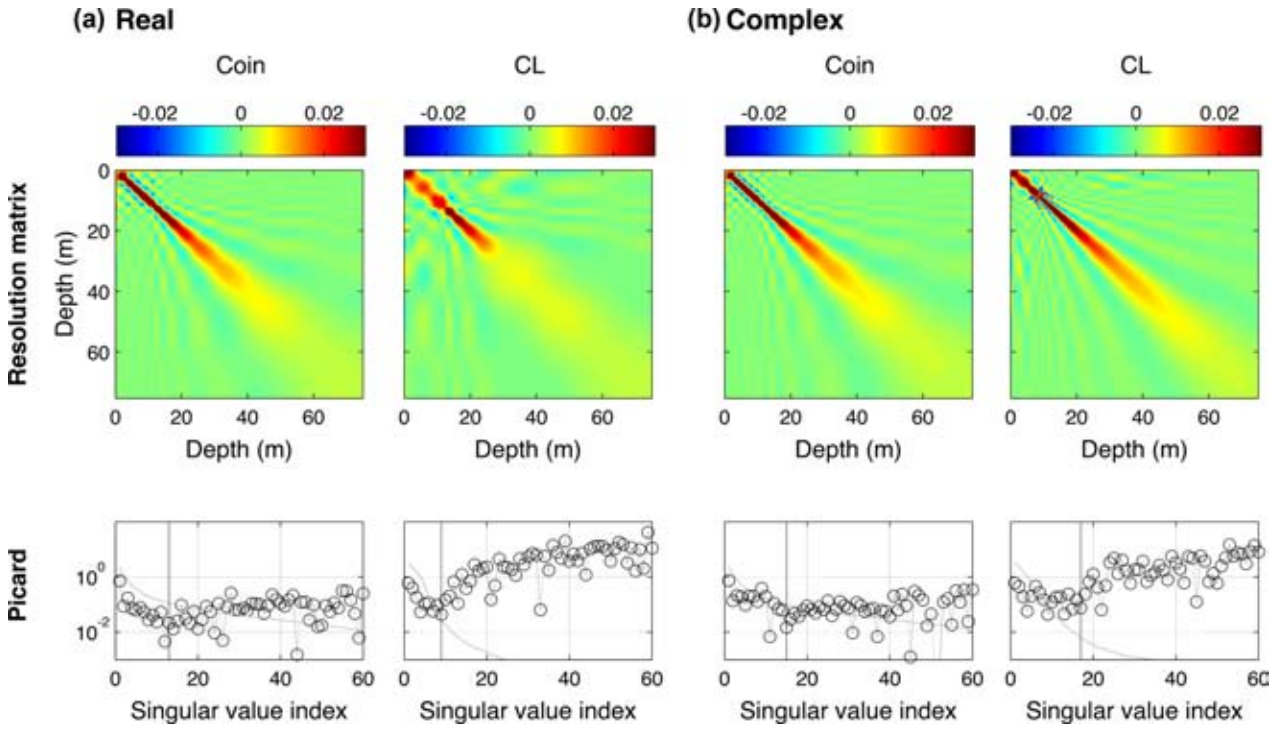

Figure 7. Model resolution matrices (row 1) and the Picard plots (row 2) for the kernel functions of Fig. 4 and for real (a) and complex (b) data. The resolution matrices are displayed as a weighting operator between the true ($\boldsymbol{m}^{\text{true}}$) and estimated ($\boldsymbol{m}^{\text{est}}$) models. The Picard plots contain the singular values (grey curves), the coefficients $|\boldsymbol{u}_i^T \boldsymbol{d}|/s_i$ (circles) and the truncation levels (black lines) for which the resolution matrices are plotted in row 1.

average decrease (for more information about the Picard plots see Fedi *et al*. [2005] and Müller-Petke & Yaramanci [2008]). For real data (Fig. 7a), resolution matrix of the coincident loop configuration suggests slightly better depth resolutions and, as expected, the resolution is significantly reduced at larger depths for both configurations. On the other hand, for complex data (Fig. 7b) it is evident that much larger depth resolution is obtainable. More importantly, the central loop resolution matrix contains similar depth resolution for shallow parts and probes deeper compared to the coincident loop resolution matrix. As discussed earlier, this improvement is a result of the geometry-driven spatial sampling of the central loop kernel.

The above-mentioned resolution matrix analysis is appropriate to assess resolution of water contents. To compare accuracy of both the water content and relaxation time parameters determined from the two configurations, we present two synthetic examples as follow. Fig. 8 shows a five-layer synthetic example comparing parameter determination of the two configurations using complex data. The true model (dotted blue lines) contains two 10-m-thick aquifers located at depths of 10 and 40 m, respectively. A water content of 0.3 m^3 m^{-3} and a relaxation time of 0.3 s were assigned to the aquifers. The layers are separated by aquitards consisting water contents of 0.05 m^3 m^{-3} and relaxation times of 0.05 s. We used a homogeneous half-space with resistivity of 100 Ωm for kernel calculation and assumed a mono-exponential model within the layers. The forward response was calculated for pulse moments and time gate values ranging from 0.08 to 12 As and from 0.04 to 0.45 s, respectively. The entire complex dataset was contaminated by 5 per cent Gaussian noise and inverted for a multilayer model. The inversion started using a homogeneous half-space model with resistivity of 100 Ωm, water content of 0.1 m^3 m^{-3} and relaxation time of 0.1 s, and a vertical constraint value of 1 was specified to tie neighbouring model parameters together (i.e. model parameters are allowed to vary around 100 per cent between neighbouring models). The same field setup as in Fig. 1 was used for simulations. Figs 8(a) and (b) display inversion results for coincident and central loop configurations, respectively. Black lines in the bottom row show estimated models and the grey area represents 68 per cent confidence intervals obtained from model parameter analysis. Rows 1 and 2 show, respectively, real and imaginary components of the observed data (columns 1, normalized), simulated data (columns 2, normalized) and data weighted residuals (columns 3). The inversion results of this synthetic example show that the central loop data are capable of resolving the true model with resolutions as good as those from the coincident loop data. Note the significant difference between signal amplitudes of the two configurations. As shown in the figure, good data fits were obtained for the two configurations (see total weighted data residuals on the plots of columns 3).

In practice due to the difficulties of describing phase of the signal, MRS data have been mostly inverted using, for example, amplitude data. Therefore, in our second synthetic example we used complex rotated amplitude data (Müller-Petke *et al*. 2011) for the same model used in Fig. 8. Similarly, we used the same field and model setup and noise data as those used in Fig. 8. The results are shown in Fig. 9 (see description of Fig. 8 for details). Again, we observe that the central-loop data resolves the true model with resolutions as good as those from the coincident loop data, with considerably higher signal amplitudes. We used AarhusInv (Auken *et al*. 2015) for inversion of our data.

We note that careful determination of instrument phase shift and employing methods to reduce the impact of frequency offset (e.g. the frequency-cycling method proposed by Grombacher *et al*. [2015]) help stabilize complex inversion of MRS data. Moreover, the shielding effect will further increase S/N of the central-loop data that leads to lower data uncertainties, compared with the coincident-loop data, and therefore lower model parameter uncertainties are expected.

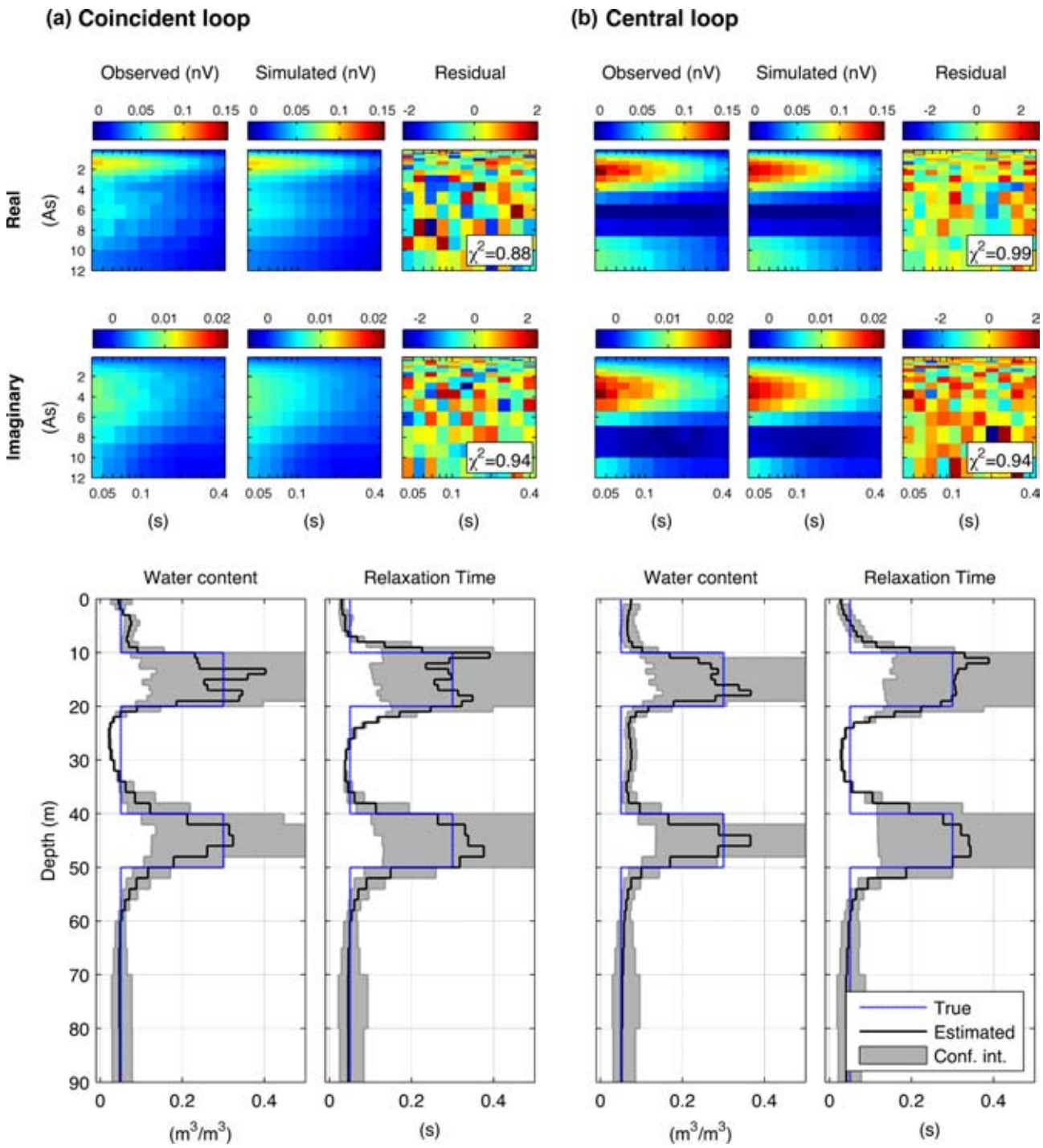

Figure 8. Inversion results of the synthetic coincident- (a) and central-loop (b) complex data. Columns 1–6 show observed data, simulated data and weighted data residuals for real (row 1) and imaginary (row 2) data. The data are normalized to the loop effective area. Note the difference in signal amplitudes. Row 3 shows inversion results in terms of water contents and relaxation times as a function of depth. Dotted blue and black lines represent the true and estimated models, respectively, and the grey area indicates the 68 per cent confidence intervals. For information of field setup and starting model see the text.

Reduced measurement dead time

One of the current limitations of the method, compared with laboratory and borehole NMR, is the relatively long effective dead time that consists of the half transmitter pulse length, instrument dead time and the post-processing time interval before the first data point (Walsh *et al*. 2011). Instrument dead time is one of the main reasons why the surface-NMR relaxation parameter differs from that of borehole-NMR data, as shown by, for example, Knight *et al*. (2012). Existing instruments used for deep groundwater investigations have measurement dead time of less than or equal to 5 ms for the GMR (Vista Clara Inc.) and 20 ms for the NUMIS (IRIS Instruments) system. In contrast to coincident loop, central loop configuration uses separate instrument channels for transmitting and receiving the NMR signal. As a result, the instrument dead

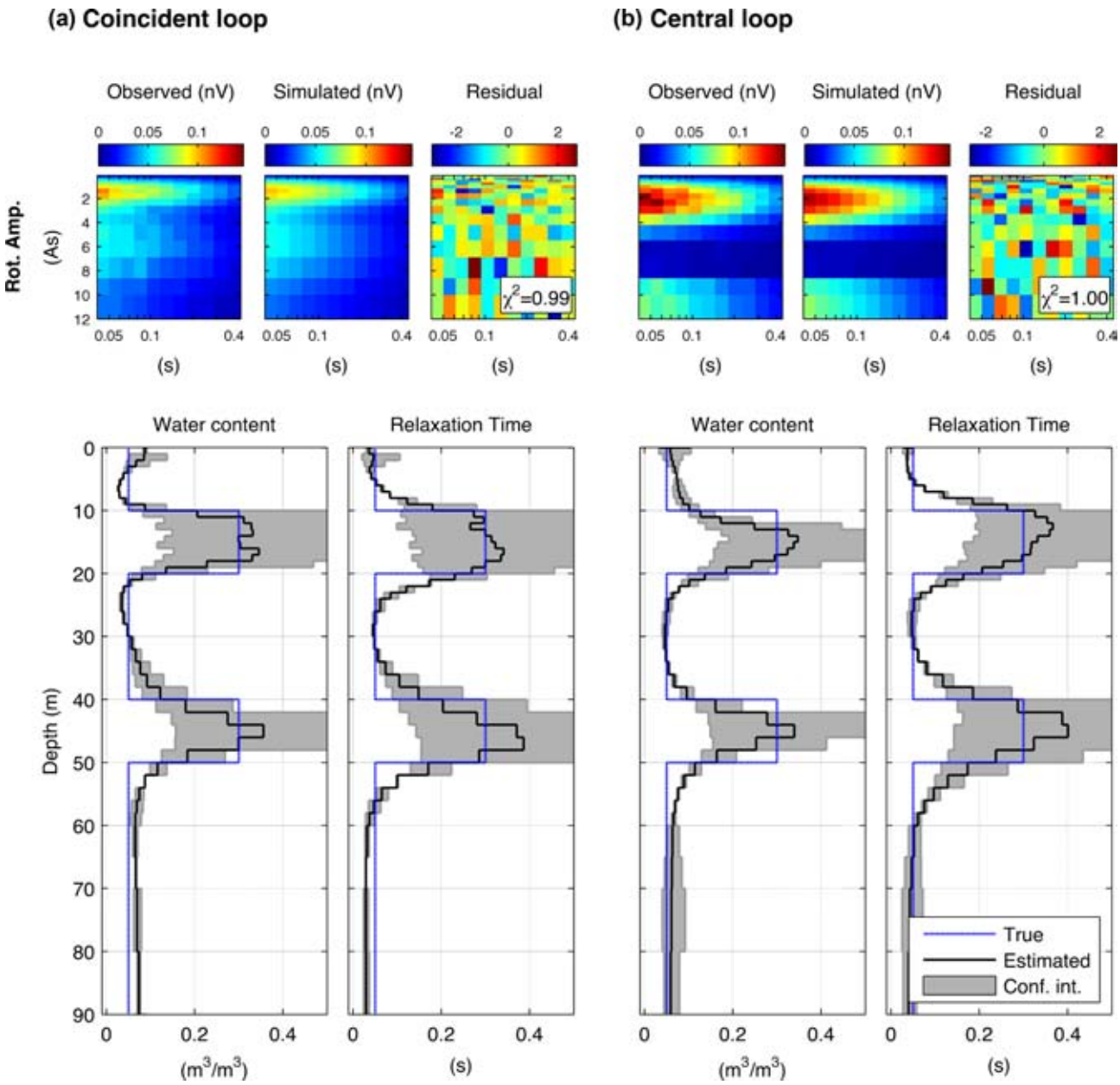

Figure 9. Inversion results of the synthetic coincident- (a) and central-loop (b) complex rotated amplitude data. Columns of row 1 show observed data, simulated data and weighted data residuals. The data are normalized to the loop effective area. Note the difference in signal amplitudes. Row 2 shows inversion results in terms of water contents and relaxation times as a function of depth. Dotted blue and black lines represent the true and estimated models, respectively, and the grey area indicates the 68 per cent confidence intervals. The same field and model setup as those of Fig. 8 were used.

time can be reduced to almost zero as it is not necessary to switch the loop from transmit to receive mode, which from a hardware point of view is a complicated operation, and which we have seen to cause problems with ringing from the switching relays. However, this advantage cannot be used by any of the current commercial available instrumentations.

FIELD EXAMPLE

To verify improved resolution of the central-loop versus the coincident-loop MRS data, we collected MRS data in the Ristrup area, Denmark. A comprehensive set of geophysical and hydrologic data have been acquired in the study area, which makes it an appropriate site for this study. Prior to data measurement, we conducted a noise survey in the area to allocate the best spot for deploying the loops. Noise condition at the site seems close to the uniform condition and is shown in row four of Fig. 6. MRS data were collected using both coincident and central loop configurations. We measured MRS data using the NUMIS Poly equipment (IRIS Instruments; four channels). Two of the channels were used as receivers while the other two channels monitored noise in the area. The MRS data contains the full FIDs, that is the voltage responses measured as a function of time and pulse moment ($V(q,t)$ in eq. (1)). The data were measured using 16 pulse moments ranging from 0.08 to 8.6 As. To ensure high quality data, measurements of the FIDs at each pulse moment were repeated 100 times and stacked together during processing. The local Earth's magnetic field had an intensity of

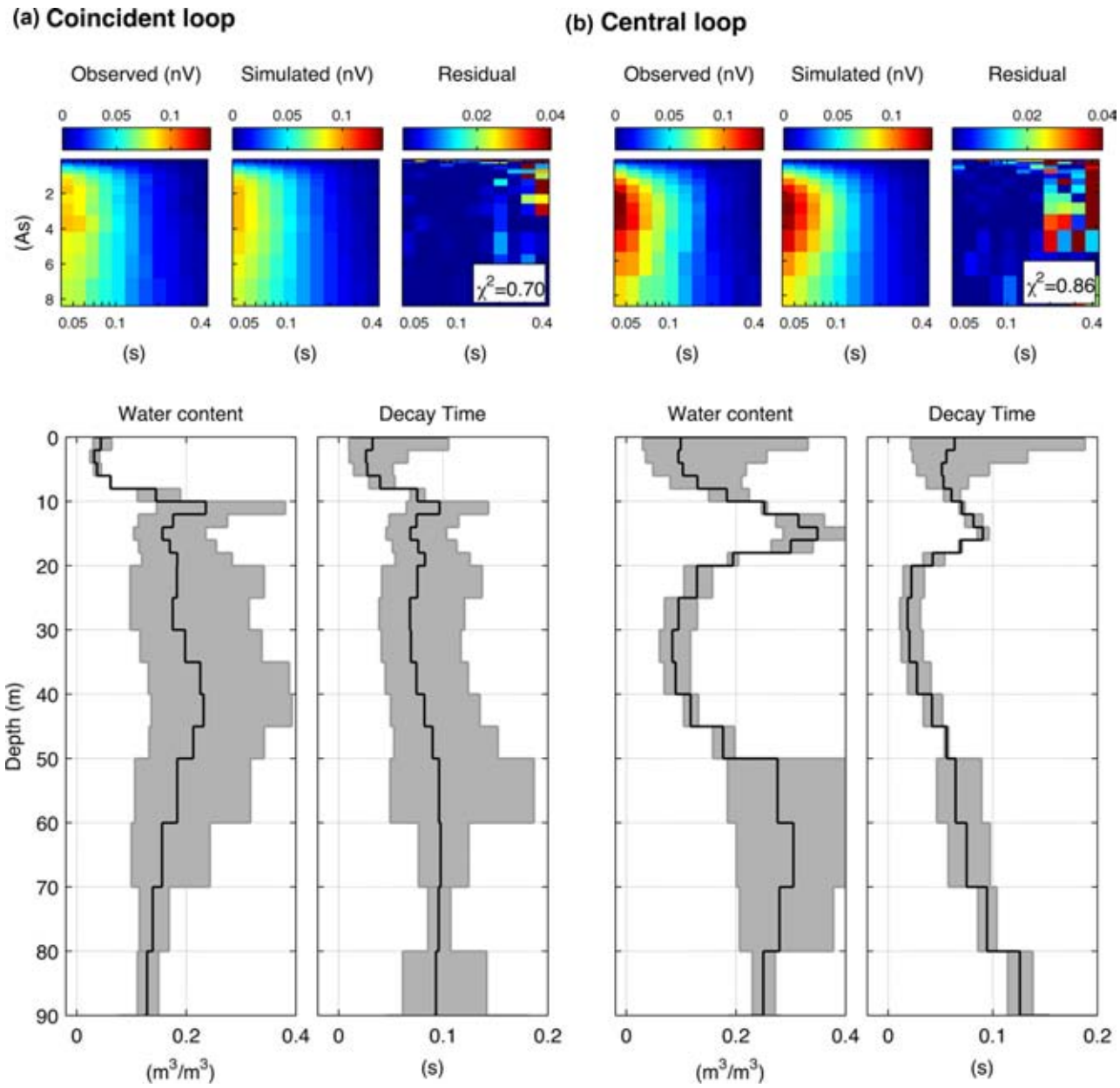

Figure 10. Inversion results of the coincident-loop (a) and central-loop (b) MRS field data. (Row 1) central- and coincident-loop MRS observed data (columns 1), simulated data (columns 2) and data weighted residuals (columns 3). The data are presented as complex rotated amplitudes and normalized to receiver effective loop area for comparison. Note the difference in signal amplitudes. (Row 2) inversion results of coincident- and central-loop MRS data in terms of water contents and relaxation times as a function of depth together with their 68 per cent confidence intervals. For information of field setup see the text.

50 303 nT and an inclination of 70°. The MRS data were processed following Dalgaard *et al*. (2012) and Larsen *et al*. (2014), and the individual FID envelopes were integrated over time gate windows to efficiently reduce noise (Behroozmand *et al*. 2012). We used complex rotated amplitude data for inversion. Airborne transient EM data, acquired using the SkyTEM system (SkyTEM Surveys Aps), were used to obtain resistivity information; the closest sounding data was selected for this study. For more information about the airborne TEM method see, for example, Schamper *et al*. (2013).

A homogeneous starting model with water content of 0.1 m^3 m^{-3} and a relaxation time of 0.1 s was used for inversion of the datasets. The MRS data sets were inverted with a smooth model, in which vertical smoothing constraints of 1 were applied to the model parameters and fixed layer boundaries were assumed during the inversion. Fig. 10 displays the inversion results of the coincident—(a) and central-loop (b) data. Row 1 shows the MRS observed data (columns 1, normalized), simulated data (columns 2, normalized) and data weighted residuals (columns 3). Both the central- and coincident-loop estimated models fit the data well (see columns 3) and total weighted data residuals of 0.86 and 0.70 are obtained. Again, note the significant difference in signal amplitudes. Row 2 shows inversion results of both coincident-loop (a) and central-loop (b) data in terms of water contents and relaxation times as a function of depth, together with their 68 per cent confidence intervals shown as grey area. The results of both configurations suggest a low water content layer with a relatively low relaxation time below the ground

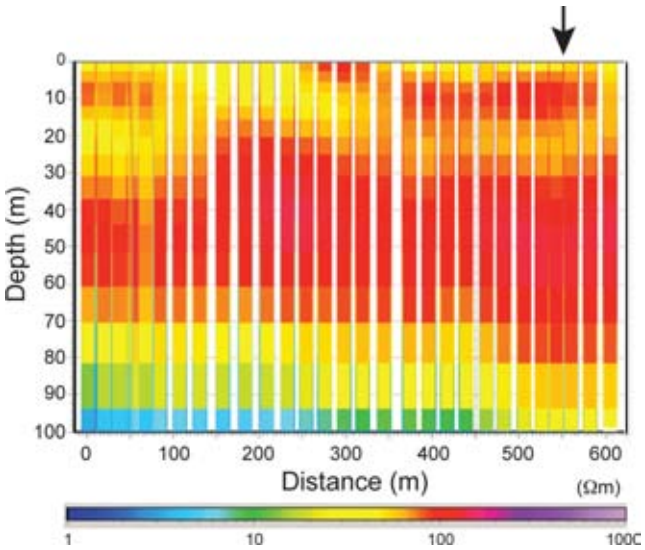

Figure 11. A southwest–northeast cross section from the inversion results of airborne-TEM data acquired in the study area. Black arrow points where the profile coincides the MRS loop. Warm and cold colours indicate resistive and conductive layers, respectively.

surface. At depths of below 10 m, a second layer (aquifer) starts, containing higher water content and relaxation time. Interpretation of the coincident-loop estimated model suggests a large aquifer with a tendency to lower water content at depths greater than 45 m. This result is in contrast to the central-loop estimated model. The central-loop data estimates a two-aquifer system; the first aquifer is separated from the second one by an aquitard layer that starts at depths of around 20 m. From a hydrologic perspective, mapping the presence of aquitards is important, since they protect groundwater resources located in deeper aquifers. The central-loop estimated model is therefore significantly different from that estimated by the coincident-loop data.

To explore which of the two inversion results represents ground truth more precisely, we compare them with complementary geophysical and borehole data. We measured the water level at the depth of ∼8 m in a borehole close to the site. This water level is in a good agreement with our estimate of the top of the first aquifer. Soil sample data are available down to a depth of 32 m that reports presence of a clay layer in the top 9.8 m followed by a sand layer (in different sizes with occasional presence of clay lenses). To validate separation of the two aquifers by an aquitard, Fig. 11 shows a depth slice through the spatially constrained inversion model of the airborne TEM data acquired in the study area. The black arrow shows the position of the MRS sounding on the profile. Based on the airborne TEM results, it is evident that two aquifers exist in the vicinity of the MRS sounding (presented by two high resistive layers shown by warm colours) that are separated by a more conductive layer, that is an aquitard.

Finally, we have compared our results with interpretations of hydrologic data from the area. Based on observations of transient head responses together with barometric data from wells in the area it is evident that the aquifer responds as a confined system with a clear barometric effect (Blaesbjerg 2006). This is also the case for interpretations of aquifer test data that show that the aquifer system acts as a confined system (Troels N. Vilhelmsen, private communication, 2015).

CONCLUSIONS

We have proposed central loop geometry as a new configuration for improved 1-D MRS investigations. Compared to the coincident loop configuration, we have demonstrated that central-loop MRS data possess different advantages as follows: (1) the central-loop kernel has a superior behaviour and its sensitivity function probes larger depth intervals over the range of pulse moments; (2) the noise level is remarkably reduced due to the usage of shielded cables making it possible to acquire MRS data in more places of interest; (3) central loop configuration often provides higher signal amplitudes; (4) the central-loop resolution matrix suggests improved model parameter estimates throughout the model space when complex data is used during inversion and (5) instrument dead time can potentially be reduced to almost zero; therefore early-time NMR signals are more obtainable.

For our field example, an increased S/N of 2.2 was achieved. This increased S/N (also shown in our synthetic examples) can be used to reduce the measurement error and the time it takes to make a measurement. Our field example verifies improved estimation obtained by central-loop MRS data, in which the central-loop inversion results are in a good agreement with the direct measure of the water level as well as with borehole data, complementary geophysical data and the hydrologic model of the area.

ACKNOWLEDGEMENTS

The first author was supported by funding from The Danish Council for Independent Research | Natural Sciences. The field data was acquired as part of the Danish Council of Strategic Research Project titled ‘HyGEM-integrating geophysics, geology and hydrology for improved groundwater and environmental management’. We would like to acknowledge Jakob J. Larsen for fruitful discussions on the noise reduction of the shielded coils. We are also thankful to Esben Dalgaard for his help in the field and to Troels N. Vilhelmsen for providing hydrologic information of the field example. We thank Mike Müller-Petke and an anonymous reviewer for their comments that helped improve the quality of the manuscript.

REFERENCES

Auken, E. *et al.*, 2015. An overview of a highly versatile forward and stable inverse algorithm for airborne, ground-based and borehole electromagnetic and electric data, *Expl. Geophys.,* **46**(3), 223–235.

Behroozmand, A.A., Auken, E., Fiandaca, G., Christiansen, A.V. & Christensen, N.B., 2012. Efficient full decay inversion of MRS data with a stretched-exponential approximation of the T2* distribution, *Geophys. J. Int.,* **190**(2), 900–912.

Behroozmand, A.A., Dalgaard, E., Christiansen, A.V. & Auken, E., 2013a. A comprehensive study of parameter determination in a joint MRS and TEM data analysis scheme, *Near Surf. Geophys.,* **11**(5), 557–567.

Behroozmand, A.A., Fiandaca, G. & Auken, E., 2013b. On the sensitivity analysis of separated-loop MRS data, in *Proceedings of the AGU Fall Meeting*, San Francisco, CA.

Behroozmand, A.A., Keating, K. & Auken, E., 2015. A review of the principles and applications of the NMR technique for near-surface characterization, *Surv. Geophys.,* **36,** 27–85.

Blaesbjerg, H., 2006. Opstilling af grundvandsmodel for Ristrup Kildeplads ud fra geologiske og geofysiske data samt kalibrering ved hydrologiske og hydrauliske data, *Master thesis,* Aarhus University, Denmark.

Braun, M., Hertrich, M. & Yaramanci, U., 2005. Study on complex inversion of magnetic resonance sounding signals, *Near Surf. Geophys.,* **3**(3), 155–163.

Dalgaard, E., Auken, E. & Larsen, J.J., 2012. Adaptive noise cancelling of multichannel magnetic resonance sounding signals, *Geophys. J. Int.,* **191**(1), 88–100.

Dalgaard, E., Christiansen, P., Larsen, J.J. & Auken, E., 2014. A temporal and spatial analysis of anthropogenic noise sources affecting SNMR, *J. appl. Geophys.,* **110,** 34–42.

Davis, A.C. & Macnae, J.C., 2012. Modelling NMR signal for compact sensors, in *Proceedings of the 5th International Meeting on Magnetic Resonance,* Hanover, Germany, p. 20.

Fedi, M., Hansen, P.C. & Paoletti, V., 2005. Analysis of depth resolution in potential-field inversion, *Geophysics,* **70**(6), A1–A11.

Grombacher, D., Müller-Petke, M. & Knight, R., 2015. Frequency-cycling for compensation of off-resonance effects and improved stability of complex inversions in surface NMR, in *Proceedings of the 6th International Workshop on Magnetic Resonance,* Aarhus, Denmark.

Hertrich, M., 2008. Imaging of groundwater with nuclear magnetic resonance, *Prog. Nucl. Mag. Res. Spectrosc.,* **53**(4), 227–248.

Hertrich, M., Green, A.G., Braun, M. & Yaramanci, U., 2009. High-resolution surface NMR tomography of shallow aquifers based on multi-offset measurements, *Geophysics,* **74**(6), G47–G59.

Jiang, C., Müller-Petke, M., Lin, J. & Yaramanci, U., 2015. Magnetic resonance tomography using elongated transmitter and in-loop receiver arrays for time-efficient 2-D imaging of subsurface aquifer structures, *Geophys. J. Int.,* **200**(2), 824–836.

Knight, R. *et al.*, 2012. Field experiment provides ground truth for surface nuclear magnetic resonance measurement, *Geophys. Res. Lett.,* **39**(3), L03304, doi:10.1029/2011GL050167.

Larsen, J.J., Dalgaard, E. & Auken, E., 2014. Noise cancelling of MRS signals combining model-based removal of powerline harmonics and multichannel Wiener filtering, *Geophys. J. Int.,* **196**(2), 828–836.

Legchenko, A., Ezersky, M., Girard, J.-F., Baltassat, J.-M., Boucher, M., Camerlynck, C. & Al-Zoubi, A., 2008. Interpretation of magnetic resonance soundings in rocks with high electrical conductivity, *J. appl. Geophys.,* **66**(3–4), 118–127.

Müller-Petke, M., Dlugosch, R. & Yaramanci, U., 2011. Evaluation of surface nuclear magnetic resonance-estimated subsurface water content, *New J. Phys.,* **13**(9), 095002, doi:10.1088/1367-2630/13/9/095002.

Müller-Petke, M. & Yaramanci, U., 2008. Resolution studies for magnetic resonance sounding (MRS) using the singular value decomposition, *J. appl. Geophys.,* **66**(3–4), 165–175.

Nyboe, N.S. & Sørensen, K., 2012. Noise reduction in TEM: presenting a bandwidth- and sensitivity-optimized parallel recording setup and methods for adaptive synchronous detection, *Geophysics,* **77**(3), E203–E212.

Ott, H.W., 1988. *Noise Reduction Techniques in Electronic Systems,* 2nd edn, Wiley.

Schamper, C. *et al.*, 2013. Airborne transient EM methods and their applications for coastal groundwater investigations, in *Groundwater in the Coastal Zones of Asia-Pacific,* p. 380, Springer Science & Business Media.

Trushkin, D.V., Shushakov, O.A. & Legchenko, A.V., 1994. The potential of a noise-reducing antenna for surface NMR groundwater surveys in the earth's magnetic field, *Geophys. Prospect.,* **42**(8), 855–862.

Walsh, D.O., Grunewald, E., Turner, P., Hinnell, A. & Ferre, P., 2011. Practical limitations and applications of short dead time surface NMR, *Near Surf. Geophys.,* **9**(2), 103–111.

Weichman, P.B., Lavely, E.M. & Ritzwoller, M.H., 2000. Theory of surface nuclear magnetic resonance with applications to geophysical imaging problems, *Phys. Rev. E - Stat. Phys., Plasmas, Fluids, Relat. Interdiscipl. Top.,* **62**(1B), 1290–1312.